Influence of bandwidth and dopant profile on quantum interference from superlattice transport studies

W. Szott, C. Jedrzejek,* and W. P. Kirk
NanoFAB Center, Department of Physics, Texas A&M University, College Station, Texas 77843-4242
(Received 14 August 1992; revised manuscript received 19 April 1993)

Measurements of quantum corrections to the magnetoconductivity in two superlattice samples of $GaAs/Al_xGa_{1-x}As$ differing in the $Al_xGa_{1-x}As$ alloy composition (and therefore in the miniband width) are reported. The sample with a smaller bandwidth displayed a larger correction to the magnetoconductivity; however, this result cannot be described by a two-dimensional theory. Using both a systematic and a detailed analysis of the transport data, we find that weak-localization (WL) rather than electron-electron interactions dominates the quantum transport corrections. An extensive quantitative interpretation of the transport results is done with an advanced weak-localization theory for superlattices, incorporating dopant distribution, wave-function modulation, and a higher magnetic-field range beyond the eikonal approximation. However, this advanced theory still assumes a δ-function impurity scattering potential. The theoretical fits to the data are not compatible with the as-grown impurity profiles, but are best fit with an effective uniform impurity distribution. While silicon dopant migration smears the impurity profile, we think some effect comes from the inadequacy of the point-scattering assumption commonly adopted in WL theory, which suggests that the long-range potential scattering in WL effects is operative.

I. INTRODUCTION

Weak localization (WL) is caused by quantum interference of the conduction electrons undergoing diffusive scattering from defects in a system.[1,2] In epitaxially grown heterojunctions the short-range scattering due to interface roughness is negligible and it is assumed that the scattering comes from doping impurities placed in the barriers. In the case of superlattices with the same mean free path as the superlattice spacing it is not obvious that the ionized impurities dominate interface roughness scattering. Surface roughness can be simulated by placing scattering centers at the interface (as we do in this paper), so that only potential scattering is considered.

Although the theory of WL can be formulated for a general impurity potential, WL corrections to conductivity have only been derived for δ-type point-scattering centers. This assumption might be adequate for metal film systems where very strong screening exists, but it is clearly suspect for semiconductor systems.

Part of the appeal of the WL theory is that it is material independent, neglects band-structure details, and makes contact with system properties through phenomenological parameters. This leaves a great deal of freedom when describing gross features and gives the possibility for quantitative "agreement" between theory and experiment. (The qualitative agreement is beyond doubt.)

Future progress in the subject relies on studying systems where more detailed microscopic information is available. Specifically, in this paper we consider superlattices with as-grown controlled impurity distributions. We have studied magnetoconductivity in two samples with potential barriers of different heights and therefore of different miniband widths. This feature determines the electron wave-function penetration into classically forbidden regions and consequently an effective impurity scattering range. Throughout the paper we stress the bandwidth dependence of the conductivity. The measured temperature dependence of the Hall constants and zero-field conductivity exclude a significant contribution from the interaction effect. The electron-electron interaction theory predicts that the temperature changes of the conductivity have an opposite sign to those of the Hall constants in contradiction to the observed data. Also, the temperature dependence of the zero-field conductivity data corroborates the magnetoconductivity results and rules out the applicability of two-dimensional (2D) theory. Finally, we compare the experimental results with a recent theory that incorporates the superlattice structure in the z direction by taking into account impurity profile and electron wave-function modulation. This theory, however, still assumes a pointlike scattering mechanism. From comparisons of the experimental results with the theoretical predictions, we conclude that the assumption of a pointlike scattering is not compatible with the experimental data if the nominal (as-grown) dopant distribution is assumed. We make this statement on the basis of careful measurements and the use of state-of-the-art WL theory.

The above-mentioned disagreement can be ascribed to two factors. The real dopant distribution is much broader compared to the nominal one due to silicon dopant migration.[3–6] The second factor is the importance of a weakly screened, long-range potential for ionized-impurity scattering that has long been established in classical transport.[7] In order to address these points, we have organized this paper as follows. In Sec. II the characteristics of the superlattice samples are presented and experimental procedures are described. Section III ad-

0163-1829/93/48(12)/8963(17)/$06.00

dresses the Hall constant as a function of magnetic field and temperature. In Sec. IV we present the magnetoresistance data and analyze it with superlattice specific models. Also, the theoretical analysis of the magnetoconductivity allows us to determine the dephasing time as a function of temperature. In Sec. V we present zero-field conductivity measurements, and we close with conclusions in Sec. VI.

II. SUPERLATTICE SAMPLES AND EXPERIMENTAL PROCEDURE

Transport measurements presented in this paper were performed on two n-type GaAs/$Al_xGa_{1-x}As$ superlattices designated as SLN and SLW [N indicates high barrier (*narrow* miniband) and W low barrier (*wide* miniband)]. They were grown by molecular-beam epitaxy (MBE) on a semi-insulating Cr-doped GaAs substrate with a 120-nm undoped GaAs buffer. The superlattices consisted of 30 periods of four layers each: 18.8-nm undoped GaAs, 1.0-nm undoped $Al_xGa_{1-x}As$ spacer, 1.8-nm $Al_xGa_{1-x}As$ doped with Si (1.0×10^{24} m^{-3}), and 1.0-nm undoped $Al_xGa_{1-x}As$ spacer. A 100-nm undoped GaAs cap layer was deposited on the top of the superlattice structure. The cross-sectional view of a representative superlattice structure is shown schematically in Fig. 1. The alloy composition was $x = 0.3$ in SLN and $x = 0.1$ in SLW. An x-ray scan[8] performed on SLN gave a measured superlattice period of 22.3 nm which agrees very well with the nominal value of 22.6 nm expected from the MBE growth conditions.

The samples were patterned into Hall bars consisting of three (for SLN) and two (for SLW) pairs of voltage probes. This geometry corresponds to transport studies in the direction parallel to the layered structure. Lateral sizes of the samples are 9.06×1.225 mm and 0.720×0.125 mm for SLN and SLW, respectively. The Hall bar structures were fabricated by standard lithography and chemical etching. Gold wire leads were bonded to $Au_xGe_{1-x}Ni$ alloyed metal Ohmic contacts.

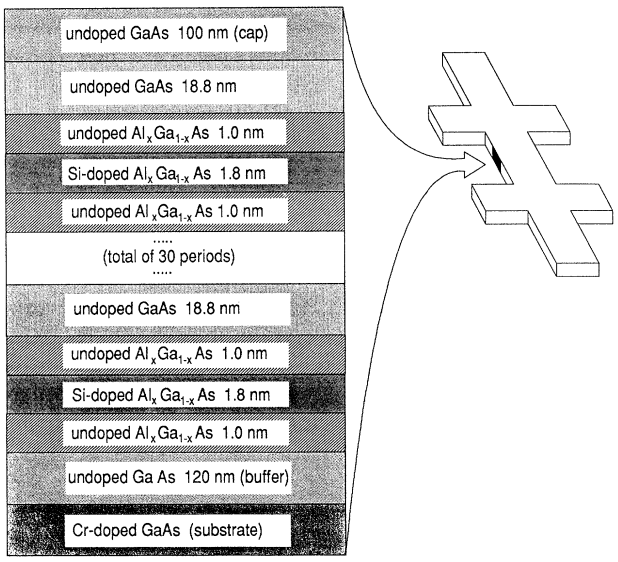

FIG. 1. Cross-sectional view of the superlattice structure.

At the interfaces between GaAs and $Al_xGa_{1-x}As$ layers, conduction- and valence-band discontinuities develop due to differences in the band gaps and electron affinities of the two materials. Recent studies[9] have determined that the conduction-band offset ΔE_c (in terms of the band-gap difference ΔE_g) is $\Delta E_c = 0.63\Delta E_g$ in the low-x, direct-gap region. This yields $\Delta E_c = 0.82x$ (eV) based on commonly accepted band-gap values and $\Delta E_g = 1.3x$ (eV). Hence, the mismatch in the conductance-band edges of the superlattice component layers is found to be $\Delta E_c = 0.246$ (0.082) eV in SLN (SLW). [Note: for the remainder of the paper when two symbols are given in which one appears in parentheses, the first (second) refers to SLN (SLW).]

It has been reported[10] that the miniband widths and band-edge values from the Krönig-Penney model for GaAs/$Al_{0.3}Ga_{0.7}As$ superlattices (but for larger miniband widths than in our samples) are within 10% of the values obtained from a more accurate $\mathbf{k} \cdot \mathbf{p}$ method.

In our case the band structure and dispersion relations in the superlattices were calculated using the Krönig-Penney model[11–13] with the following parameters: electron effective mass $m = 0.0667m_0$ (where m_0 is the free-electron mass), the barrier height $V_b = 0.246$ (0.082) eV, the barrier width is 3.8 nm, and the well width is 18.8 nm. The dispersion relations are very flat and, in the case of the ground miniband, can be accurately described by the tight-binding formula, viz.,

$$\epsilon_z(k_z) = w[1 - \cos(k_z a)], \tag{1}$$

where a is the superlattice constant and w is the miniband half-width.

The ground miniband is located 12.0 (7.5) meV above the potential minima. Its width $2w$ is found to be 1.12 (4.05) meV. The first excited miniband is formed at the relatively large energy of 44.3 (30.3) meV and is approximately four times wider [14.0 (4.90) meV] than the ground miniband. The Fermi energy is calculated from the resulting density of states and found to be 17.1 (13.8) meV (for the measured density of carriers given in Table I). The Fermi level lies in the middle of the band gap between the first two minibands. Its distance

TABLE I. Superlattice parameters.

Parameter	SLN	SLW
V_b (eV)	0.246	0.082
$2w$ (meV)	1.12	4.05
n ($\times 10^{23}$ m^{-3})	2.03	1.47
E_F (meV)	17.1	13.8
k_F (nm^{-1})	0.173	0.155
μ ($m^2 V^{-1} s^{-1}$)	0.646	0.551
τ_e (ps)	0.224	0.190
ℓ_e (nm)	67.2	51.3
$k_F \ell_e$	12	7.9
$D_\parallel$ ($cm^2 s^{-1}$)	1.0×10^2	6.9×10^1
B_e (T)	0.073	0.125

from the first excited band is large enough (> 9 meV) so that the transport contributions from the excited bands are negligible at low temperatures ($kT \leq 1$ meV). On the other hand, the Fermi level is located high (> 9 meV) above the top of the ground miniband which is a typical situation in highly or moderately doped superlattices. Consequently, the Fermi surface has an almost cylindrical shape. This fact simplifies the analysis of the weak-localization effects in superlattices and was employed in the development of the theoretical models in Refs. 14–16.

The carrier densities in the superlattices under consideration were determined from low-temperature Hall measurements. The average Hall constant in the field interval $(-0.1, +0.1)$ T yields $n = 2.03\ (1.47) \times 10^{23}$ m^{-3} assuming a thickness of $30 \times (18.8\ \text{nm} + 3.8\ \text{nm})$. The Hall mobilities are found to be $\mu = 0.64\ (0.55)$ m^2 V^{-1} s^{-1}.

All the basic parameters of the superlattices introduced and discussed above are listed in Table I, which also contains the following entries: elastic-scattering time τ_e (from the classical Drude formula), the electron mean free path ℓ_e, the disorder parameter $k_F \ell_e$, the parallel (to the superlattice layer structure) diffusion constant $D_\parallel$, and the characteristic field for elastic scattering

$$B_e = \frac{\hbar}{4eD_\parallel \tau_e}. \tag{2}$$

All the data presented in this paper were taken by a pulsed dc current technique and an automatic data acquisition system. A programmable current source connected to the sample source and drain electrodes was used to send short (500 ms), low-amplitude (1–5 μA), positive-polarity square pulses of dc current through the sample. Four digital voltmeters connected to various pairs of voltage probes around the sample (two for longitudinal voltages V_{xx} and two for transverse voltages V_{xy}) were triggered to read near the end of each current pulse. This sequence was then repeated with a negative-polarity current pulse. Bipolar pulses were used to eliminate thermal emfs. After about 1 s of settling time, this cycle of plus and minus current pulses was repeated to obtain another data point. In the magnetotransport experiments the magnetic field was typically continuously changing at a constant rate of the order of 30 mT/min while the data were being taken.

The zero-field resistivity measurements were characterized by a large number of points (on the order of 1000). Statistical analysis of this data resulted in a standard deviation of $\approx 1 \times 10^{-4}$ of the measured voltage for a single data point. This corresponded to an absolute error of 100 nV which was equivalent to the resolution of the voltmeters (in the $5\frac{1}{2}$ digit mode). This value was used to determine the input data error in the analysis of the magnetotransport results.

III. HALL EFFECT

Hall voltage measurements of the GaAs/Al$_x$Ga$_{1-x}$As superlattices were performed by the standard technique for bridge-type samples while collecting magnetoresistance data. For reasons discussed below, only low-field results are relevant and are presented here. Figure 2 shows examples of the Hall resistivity data at selected temperatures for SLN and SLW, respectively. Experimental points are represented by small squares and only every third point is shown for clarity. The approximate linear behavior of ρ_{xy} as a function of the magnetic field is clearly seen. In order to study the Hall resistance in more detail, the derivative of ρ_{xy} with respect to the magnetic field B was calculated numerically. Due to the statistical error (of the order of $1 \times 10^{-8}\ \Omega$ m) direct differentiation of the data produced significant scatter in the results, thus obscuring interesting features in ρ_{xy}. Therefore, a smoothing procedure was first applied. The solid lines through the experimental points are the results of a standard cubic spline smoothing routine. The extent of smoothing, measured by standard chi-squared statistics (χ^2), was determined from the number of data points ($\chi^2 = N$) with uncertainty given by $\sigma(\chi^2) = \sqrt{2N}$. The derivative $\frac{\partial \rho_{xy}}{\partial B}$ was then calculated for the smoothed data and is shown in the same figures. Error bars added to those plots represent the uncertainty of $\frac{\partial \rho_{xy}}{\partial B}$ given by $\sigma(\chi^2)$. This procedure was applied to the data sets at

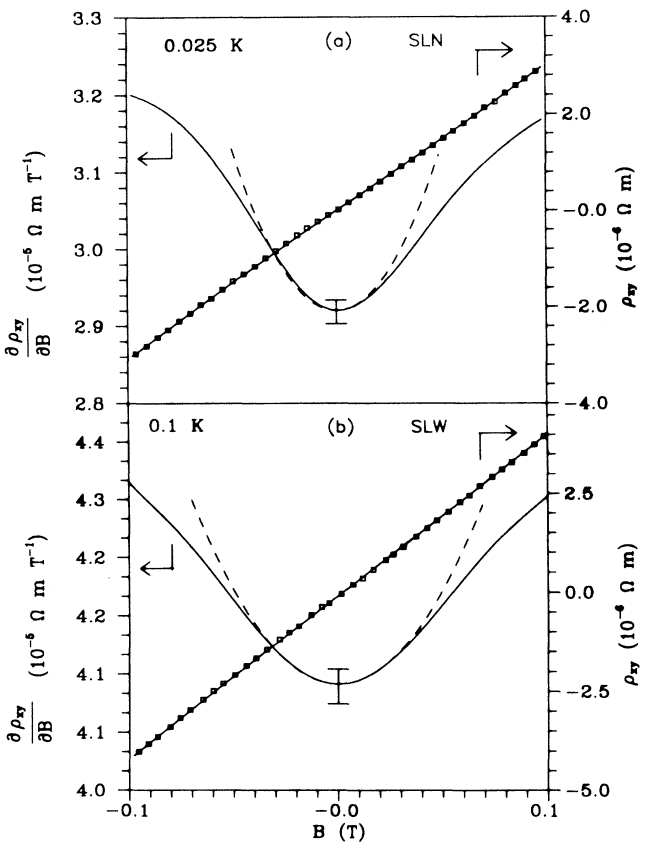

FIG. 2. Hall resistivity ρ_{xy} and differential Hall constant $\frac{\partial \rho_{xy}}{\partial B}$ vs magnetic field B for SLN at $T = 0.025$ K (a) and SLW at $T = 0.1$ K (b). Squares represent data points. Solid curves result from data smoothing. The error bars represent the uncertainty of the smoothed values. The dashed curves are low magnetic-field fits of the semiclassical theory to the experimental results.

various temperatures. Thus the temperature dependence of the derivative $\frac{\partial \rho_{xy}}{\partial B}$ was determined and is presented in Fig. 3 for SLN (a) and SLW (b), respectively. Here, the data is plotted for constant values of $B = 0$ and $B = B_{\max}$, where $B_{\max}$ is the maximum field for which the magnetoresistance data will be analyzed in the next section. $B_{\max} = 0.03$ (0.06) T.

The results introduced above for the differential Hall constant, $R_H \equiv \frac{\partial \rho_{xy}}{\partial B}$, show positive changes of R_H for both the increasing magnitude of magnetic field B and temperature T. These changes are remarkable notwithstanding relatively large errors of $\approx 1\%$. For example, R_H increases by 10% when the magnetic field changes from $B = 0$ T to $B = 0.1$ T in SLN; similarly, a 7.5% difference in $R_H(B = 0)$ is observed for temperature changes from $T = 0.02$ K to $T \approx 20$ K in SLW. In order to analyze this behavior of R_H, one has to take into consideration three possible effects: (i) the semiclassical effect; (ii) the weak-localization effect; and (iii) the electron-electron interaction effect.

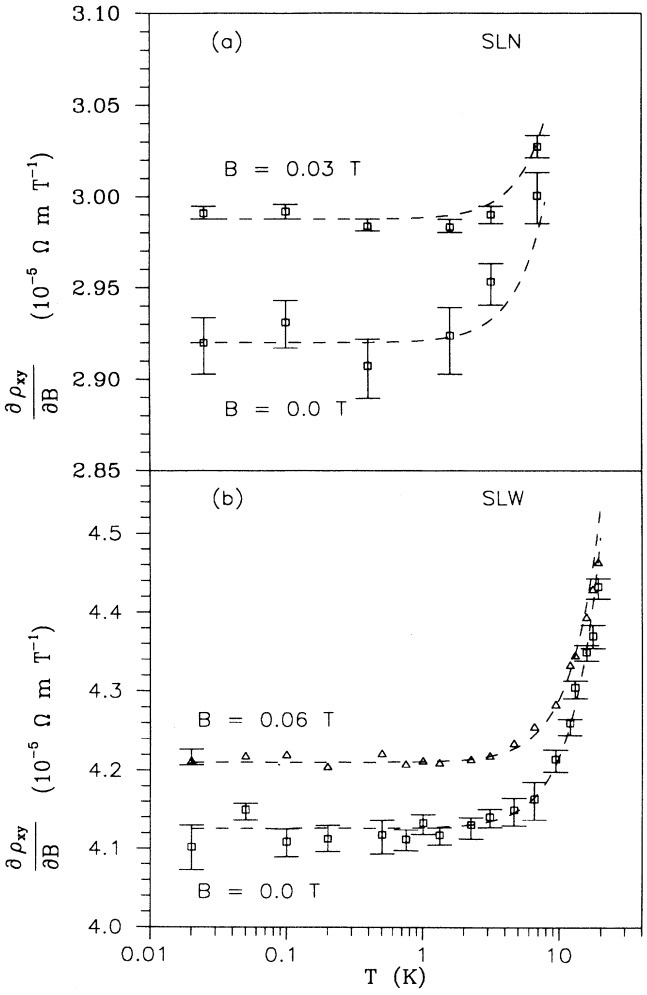

FIG. 3. The differential Hall constant $\frac{\partial \rho_{xy}}{\partial B}$ as a function of temperature T at fixed values of the magnetic field B in SLN (a) and SLW (b). Dashed curves represent best fits of semiclassical results to experimental data.

A. Semiclassical effect

This effect manifests itself as a correction to R_H through a scattering factor r_H defined by the equation

$$\rho_{xy} = \frac{B}{en} r_H, \tag{3}$$

for one type of charge carrier with density n. This factor is, in general, a complicated function of doping, temperature, and magnetic field. However, for metallic systems such as doped superlattices, at temperatures T much below the Fermi temperature T_F, with impurity scattering as a dominating scattering process, and in the limit of classically weak magnetic fields $\omega_c \tau = \mu B \ll 1$, the scattering factor r_H is given by the following formula obtained via the standard Sommerfeld expansion[17]

$$r_H = C_0 + C_1 \left(\frac{T}{T_F}\right)^2 + C_2 (\mu B)^2, \tag{4}$$

where coefficients C_i, $i = 0, 1, 2$ are of order unity and result from the anisotropy and energy dependence of the scattering process involved. For example, in the model discussed in Ref. 14, where the scattering time $\tau(\mathbf{p}) = \tau_0 \left[1 + b \cos(p_z a)\right]^{-1}$, these coefficients are found to be

$$\begin{aligned} C_0 &= \frac{1}{\sqrt{1-b^2}}, \\ C_1 &= \frac{\pi^2}{6} 2\eta \left[\frac{2\eta + 1}{\sqrt{1-b^2}} - (1+\eta)\right], \\ C_2 &= \frac{1+b^2}{1-b^2} - \frac{1}{2} \frac{1}{\sqrt{1-b^2}} \frac{2-3b^2}{1-b^2}, \end{aligned} \tag{5}$$

where it was assumed that $\tau_0(E) \propto E^\eta$. The differential Hall constant $R_H = \frac{\partial \rho_{xy}}{\partial B}$ acquires a similar form

$$R_H = \frac{1}{en} \left[C_0 + C_1 \left(\frac{T}{T_F}\right)^2 + 3C_2 (\mu B)^2\right]. \tag{6}$$

Field dependence. According to the above formula, the Hall constant R_H is a quadratic function of magnetic field B. For small fields this type of behavior is actually observed in the superlattices studied here (see Fig. 2). However, the experimental results can be quantitatively explained by the semiclassical effect only if large values of the scattering anisotropy factor b are assumed. The dashed parabolas in Fig. 2 were obtained using the estimated mobilities [$\mu = 0.646$ (0.551) m^2 V^{-1} s^{-1}] and adjusting the anisotropy factor b, which was found to be $b = 0.94$ (0.90). These large values are not consistent with the magnetoresistance data, which will be discussed in Sec. IV C . On the other hand, this disagreement implies that a more complete analysis requires the quantum effects be included.

Temperature dependence. At temperatures low compared to the Fermi temperature, the Hall constant increases quadratically with temperature. Although carrying relatively large errors, the experimental results follow closely a T^2 dependence as shown in Fig. 3. The dashed curves in these figures were calculated using the formula

$$R_H = R_H(T=0)\left[1 + C_1\left(\frac{T}{T_F}\right)^2\right]. \quad (7)$$

Here, the scattering anisotropy factor is neglected ($b = 0$) and the Fermi temperature $T_F = 198$ (160) K corresponds to the Fermi energy $E_F = 17.1$ (13.8) meV. Thus, the exponent η, which determines the energy dependence of the scattering time, was found to be $\eta = 2.2$ (1.3) at $B = 0$. At finite magnetic fields the temperature dependence of the Hall constant is reduced. At $B = B_{\max}$ we find the exponent that fits the data best is 1.9 (1.2).

The processes of electron scattering from ionized impurities in superlattices have not been studied so far. Therefore, a direct comparison with a theory and/or other experiments is not possible at this time. In 3D systems with randomly distributed impurities, η varies between 1.5 for weakly screened potentials down to 0 for completely screened impurities.[18] The situation is even more complicated in the case of 2D systems, where the scattering centers are usually displaced from the plane of the 2D electron gas.[4] For remote impurities, the scattering time τ is typically a linear function of the electron energy, while closely located scattering centers result in $\tau \propto E^{\frac{3}{2}}$.

The exponent $\eta = 1.3$ found in SLW falls into the range stated above for 2D systems as well as three-dimensional (3D) ones. SLN exhibits a larger exponent $\eta = 2.2$. This superlattice is characterized by a narrower miniband (1.12 meV vs 4.05 meV in SLW); electrons are more localized in the well regions, and consequently ionized donors intentionally doped in the barriers cannot be screened as effectively as those in wide-miniband superlattices. This qualitatively explains the difference in the exponent η. However, it is not clear whether this large value of η can be completely ascribed to the semiclassical effect discussed here.

B. Weak localization

A weak-localization theory of the Hall effect has been developed for small magnetic fields.[19] Off-diagonal elements of the conductivity tensor required for the Hall constant R_H were calculated in the linear-response approximation to the external fields $(\mathbf{E}, \mathbf{B})$. This procedure provides only the zero-field limit of $R_H(B \to 0)$. Therefore, the magnetic-field dependence of R_H cannot be studied in detail at this time. However, an important result is that weak localization predicts no correction to the Hall constant at zero field, i.e., $\Delta R_H(B = 0) = 0$, independent of the dimensionality and other particular features of a weakly localized system.[20] This may be simply interpreted as the absence of weak-localization corrections to the carrier density ($R_H = \frac{1}{en}$). The importance of this result stems from the fact that the other quantum-mechanical phenomenon described by the electron-electron interaction theory predicts significantly different behavior of the Hall effect.

C. Electron-electron interaction effect

Studies of electron-electron interactions in weakly disordered systems[19,20] have shown that the Hall conductivity remains unperturbed by this effect, i.e., $\Delta\sigma_{xy} = 0$. Consequently, the Hall constant as $B \to 0$ is modified according to

$$\frac{\Delta R_H}{R_H} = -2\frac{\Delta\sigma_{xx}}{\sigma_{xx}}\frac{1}{1-(\omega_c\tau)^2}. \quad (8)$$

This relation was investigated experimentally and confirmed in Si metal-oxide-semiconductor field-effect transistors (MOSFET's),[21] where the positive changes of the conductivity σ_{xx} with temperature and electric field were observed concomitant with the negative changes of the Hall constant.

As shown in Sec. V the superlattices studied in this work clearly demonstrate positive changes in conductivity with temperature. If these changes were caused by electron-electron interactions, then one should see the Hall constant decrease with increasing temperature—opposite to the observed behavior. Therefore, the electron-electron interaction effect is not consistent with the experimental data at low fields. Also, at the maximum fields studied here ($B \approx B_{\max}$) for which Eq. (8) is still correct, it is not plausible that the electron-electron interaction contributes significantly to the observed effects. At this field the amplitude of the temperature changes of $\Delta\sigma_{xx}$ is strongly reduced. Therefore, any possible changes of R_H due to the electron-electron interaction effect are even smaller than those at zero field. Here, the factor $[1-(\omega_c\tau)^2]^{-1}$ can be neglected since $\omega_c\tau \ll 0.01$ for $B \le B_{\max}$.

The absence of temperature-dependent corrections to the conductivity due to the electron-electron interactions implies that the contributions from exchange effects virtually cancel those from direct interactions since the two enter the conductivity formula with opposite signs.[2] Although a theory of electron-electron interactions specified for superlattices does not exist at this time, the interaction coupling constant $\tilde{F}$ can be estimated within limits set by the expressions for 2D and 3D systems, where the conductivity corrections are proportional to[2]

$$(2 - \tfrac{3}{2}\tilde{F}) \text{ in 2D} \quad \text{and} \quad (\tfrac{4}{3} - \tfrac{3}{2}\tilde{F}) \text{ in 3D}. \quad (9)$$

From the cancellation condition, mentioned above, $\tilde{F}$ is found to be $\frac{4}{3}$ in 2D and $\frac{8}{9}$ in 3D. Consequently, in the superlattice $\tilde{F}$ is expected to be of the order of unity. This value will be used to estimate corrections to the magnetoresistivity in the next section.

IV. MAGNETORESISTANCE EFFECTS

Magnetoresistance of metallic systems is normally positive.[22] This statement is quite general and based on the notion of minimizing energy dissipation. Exceptions from this general rule are found in magnetic systems where the scattering can be affected by the spin alignment.[23] Also, boundary scattering may alter the influence of the magnetic field on electron transport and cause a negative magnetoresistance.[24] In addition, the energy arguments completely neglect any correlation effects due to the quantum nature of electron transport. Therefore, negative magnetoresistance observed in

nonmagnetic systems, where boundary scattering does not significantly alter electron motion, bears evidence of quantum effects.

The $GaAs/Al_xGa_{1-x}As$ superlattices studied in this work provide an interesting example of such a system. Figure 4 presents low-temperature experimental results of the longitudinal resistivity ρ_{xx} as a function of magnetic field B for SLN and SLW, respectively. To a very good accuracy this magnetoresistivity effect is symmetric with respect to the magnetic field. The small asymmetry can be included as a linear-B component of ρ_{xx} ($\rho_{xx} \propto cB$) where $c = 3 \times 10^{-3}\ \rho_{xx}(0)\ \mathrm{T}^{-1}$ in SLN and $c = 3 \times 10^{-4}\ \rho_{xx}(0)\ \mathrm{T}^{-1}$ in SLW [$\rho_{xx}(0)$ is the zero-field resistivity]. Similarly, only a very small asymmetry of the Hall resistivity ρ_{xy} is observed at low magnetic fields (see Fig. 2). This small asymmetry implies that the voltage probes of the superlattice devices are accurately aligned. Moreover, the lack of a significant asymmetric contribution in $\rho_{xx}(B)$ is interpreted as the result of the macroscopic homogeneity of the samples. As shown in our simulations[25] even a small inhomogeneity of sample properties (such as the local density of carriers and/or the scattering rate) in the direction of the current flow result in relatively large asymmetry in $\rho_{xx}(B)$. The one-order-of-magnitude difference between the asymmetries of the two superlattices can be easily explained as due to the corresponding difference in the sizes of the samples. The larger asymmetry is observed in the bigger sample (containing more macroscopic inhomogeneities) of SLN, where the size of the effective area is 2.54 mm × 1.27 mm as compared to the 0.24 mm × 0.125 mm area for SLW.

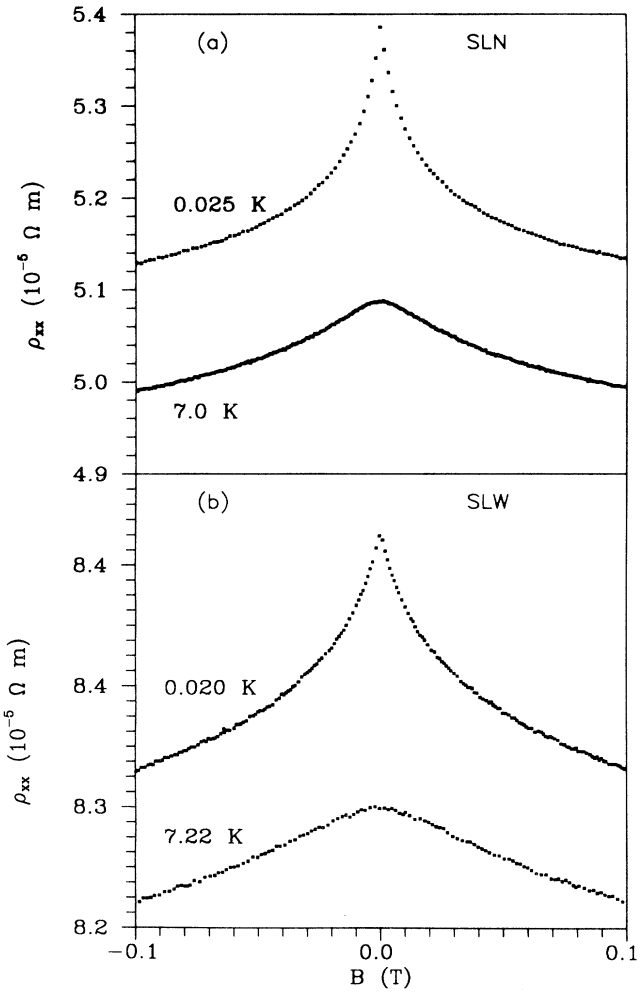

FIG. 4. Longitudinal resistivity ρ_{xx} as a function of magnetic field B at selected temperatures in SLN (a) and in SLW (b).

The superlattices studied here were not intentionally doped with any magnetic atoms and the level of residual magnetic impurities is estimated to be below $1 \times 10^{20}\ \mathrm{m}^{-3}$ (see discussion in Sec. IV D), much lower than the average density of Si donors ($\approx 1 \times 10^{23}\ \mathrm{m}^{-3}$). Therefore, the negative magnetoresistance under consideration cannot be ascribed to scattering from polarized magnetic moments. Also, the boundary scattering is completely negligible in this case because the width of the devices (> 100 μm) is much larger than the electron mean free path (0.05 μm).

Consequently, the observed reduction of the resistivity with applied magnetic field should be explained in terms of quantum corrections to electron transport. Additional information about the superlattices studied here is provided by the disorder parameter $k_F l_e$ (k_F is the Fermi wave vector, l_e is the electron mean free path) which is found to be ≈ 10. This parameter measures the scattering disorder of a system and its value found here implies that the superlattices are only weakly disordered. In this regime, the weak-localization effect as well as electron-electron interaction effects (under special conditions discussed below) can result in negative magnetoresistance phenomena as has been verified in a variety of systems.[26–28] These two effects will be studied in Secs. IV A–IV D.

A. Electron-electron interactions

The mutual electron-electron interaction effect comprises several distinct corrections to the conductivity of a weakly disordered system.[2] With respect to magnetotransport, these corrections are naturally divided into spin effects and orbital effects. The spin effects become important when the magnetic field is strong enough to split the antiparallel electrons into spin-up and spin-down subbands with an energy gap of $g^*\mu_B B$ [the effective electron magnetic moment ratio, $g^* = 0.522$ for GaAs (Ref. 29)] larger than the thermal energy $k_B T$. This defines a characteristic field for the spin effects as $B_s = \frac{k_B T}{g^* \mu_B}$. For fields $B > B_s$, negative magnetoconductivity is expected.

The orbital effects also lead to negative magnetoconductivity. These effects become important when the cyclotron radius $l_m^2 = \frac{\hbar}{eB}$ becomes comparable to the thermal length $l_t^2 = \frac{\hbar D}{\pi k_B T}$ or, equivalently, for fields B greater than the characteristic thermal field $B_t = \frac{\pi k_B T}{eD}$. The orbital effects are suppressed at fields higher than the characteristic elastic field $B_e = \frac{\hbar}{4eD\tau_e}$. Typically $B_t < B_e < B_s$ and in the two nonoverlapping regions of the mag-

netic field, i.e., $B_t < B < B_e$ and $B > B_s$ the electron-electron interaction effects contribute to negative magnetoconductivity, $\Delta\sigma^i_{xx}(B \neq 0) < \Delta\sigma^i_{xx}(B = 0)$.

The behavior of the magnetoresistivity $\Delta\rho^i_{xx}(B) - \Delta\rho^i_{xx}(0)$ can be deduced from the following expression obtained by inverting the conductivity tensor and calculating first-order corrections due to $\Delta\sigma^i_{xx}$,

$$\Delta\rho^i_{xx}(B) - \Delta\rho^i_{xx}(0) = \frac{1}{\sigma_0^2}[\Delta\sigma^i_{xx}(0) - \Delta\sigma^i_{xx}(B) + (B\mu)^2\Delta\sigma^i_{xx}(B)], \quad (10)$$

where μ is the classical mobility and σ_0 is the classical conductivity at zero field. Here, the absence of corrections to the Hall conductivity was employed, $\Delta\sigma^i_{xy} = 0$. From Eq. (10) it follows that for classically weak fields ($B \ll B_c$, where by definition $B_c = \mu^{-1}$) the second term dominates, and the negative magnetoconductivity implies positive magnetoresistivity. On the other hand, in the field regions of $B < B_t$ or $B_e < B < B_s$ the electron-electron interaction effects produce field-independent corrections, so that $\Delta\sigma^i_{xx}(B) = \Delta\sigma^i_{xx}(0)$. Consequently, in these regions the magnetoresistivity acquires the simple form

$$\Delta\rho^i_{xx}(B) - \Delta\rho^i_{xx}(0) = \frac{1}{\sigma_0^2}(B\mu)^2\Delta\sigma^i_{xx}(0), \quad (11)$$

and is negative because the interactions always suppress the zero-field conductivity, $\Delta\sigma^i_{xx}(0) < 0$. However, this effect is negligible unless it occurs at large magnetic fields $B \approx B_c$.

In the samples studied here, the characteristic fields discussed above are $B_s = 2.85$ T at 1 K, $B_t = 0.027$ (0.039) T at 1 K, $B_e = 0.073$ (0.125) T, $B_c = 1.55$ (2.0) T. Hence, the electron-electron interaction effects *cannot* account for the negative magnetoresistance because it is observed in the superlattices at fields $B \leq 0.1$ T, much lower than B_c (see Fig. 4). However, it is possible, in general, that a relatively small positive magnetoresistivity from the interaction effects is superimposed on a larger negative magnetoresistivity due to weak localization. This situation is discussed below.

As is evident from the values of B_s the spin effects do not contribute to the magnetoresistivity with the possible exception of very low temperatures ($T \leq 35$ mK) and large fields ($B \geq 0.1$ T). The orbital effects require more detailed analysis. Unlike the case of weak localization which does not involve any coupling parameters, the interaction effects include coefficients which measure an effective strength of the electron-electron screened Coulomb repulsion. In particular, the magnetoresistivity corrections from the orbital effects are proportional to the following coupling constant:[2]

$$g = \frac{\tilde{F}}{2}\frac{1}{1 + \frac{\tilde{F}}{2}\ln\frac{1.13T_F}{T}}, \quad (12)$$

where $\tilde{F}$ was estimated in Sec. III C to be approximately one. At low temperatures ($T \leq 1$ K) the coupling constant g is suppressed due to the relatively large denominator, e.g., $T_F = 198$ K and $\tilde{F} = 1$ result in $g \leq 0.13$. On the other hand, at higher temperatures ($T > 1$ K) the effective range of the magnetic field in which the electron-electron interaction effects contribute substantially becomes very small as B_t approaches B_e. Consequently, at fields smaller than $\approx \frac{1}{2}B_e$, where the observed magnetoresistance effects are large, the positive magnetoresistance contribution by the electron-electron interaction effects is insignificant. For example, a 2D analysis, which significantly overestimates quantum interference effects in superlattices as shown in Sec. IV B, yields an *e-e* contribution to the magnetoconductivity that is less than 2.5% of the value measured in SLN at $T = 1.4$ K and $B = 0.03$ T. Therefore, the *e-e* interaction effects will be neglected in the subsequent analysis. The absence of the electron-electron interactions in low magnetic field and low-temperature experimental studies of magnetotransport was also observed in other systems based on GaAs/Al_xGa_{1-x}As heterostructures.[30,31]

B. Weak localization: 2D analysis

A semiconductor superlattice consisting of N periods can be approximately considered as a system of N independent, noninteracting, 2D quantum wells which, from the viewpoint of electrical transport, form a parallel array of conductors. Such an approach was adopted in the past by several groups, including those observing quantum corrections to conductivity.[32–34] Therefore, in this section the negative magnetoresistivity, as observed in the superlattices and presented in Fig. 4, will be analyzed using the theory of weak-localization in 2D. According to this theory[19,35,36] the magnetoconductivity corrections are given by

$$\Delta\sigma^{2D}_{WL}(B) \equiv \sigma^{2D}_{WL}(B) - \sigma^{2D}_{WL}(0) = \frac{e^2}{2\pi^2\hbar}\left[\psi\left(\frac{1}{2} + \frac{B_{ph}}{B}\right) - \psi\left(\frac{1}{2} + \frac{B_e}{B}\right) + \ln\frac{B_e}{B_{ph}}\right], \quad (13)$$

where the characteristic elastic field B_e was defined in Eq. (2), the characteristic dephasing field B_{ph} is given by

$$B_{ph} = \frac{\hbar}{4eD\tau_{ph}}, \quad (14)$$

where τ_{ph} is the dephasing time, and ψ is the digamma function.

The weak-localization corrections σ_{WL} are obtained by subtracting the classical conductivity from the total one,

$$\sigma_{WL} = \frac{\rho_{xx}}{\rho^2_{xx} + \rho^2_{xy}} - \frac{\rho^{cl}_{xx}}{(\rho^{cl}_{xx})^2 + (\rho^{cl}_{xy})^2}, \quad (15)$$

where the superscript "cl" refers to the classical components, and we employed $\rho_{xy} = \rho^{cl}_{xy}$ due to the vanishing weak-localization corrections to the Hall resistivity. Figures 5 and 6 show the experimental results of the quantum corrections to magnetoconductivity, $\Delta\sigma_{WL}(B) =$

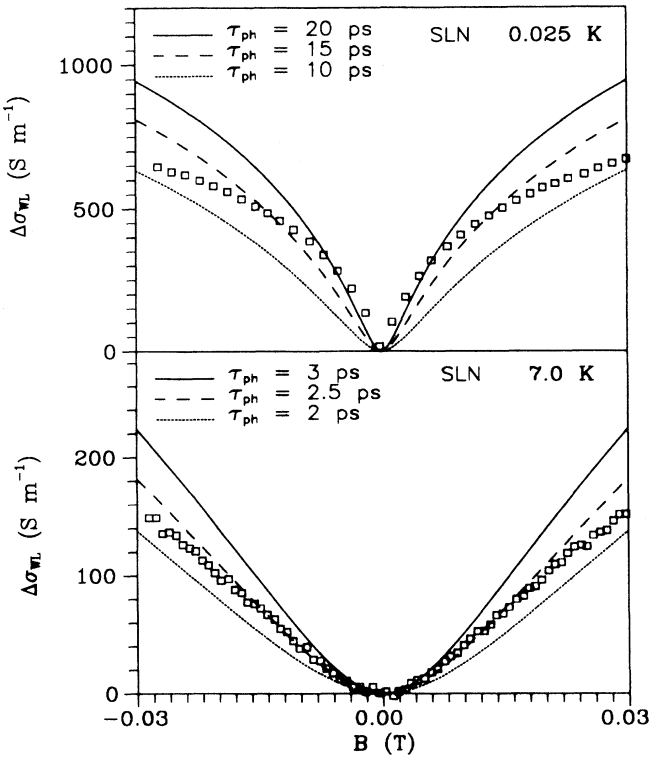

FIG. 5. Data vs the 2D theory of weak-localization corrections to magnetoconductivity in SLN at two different temperatures. Squares represent experimental points. Curves are theoretical results of weak localization in 2D calculated for different dephasing times τ_{ph}.

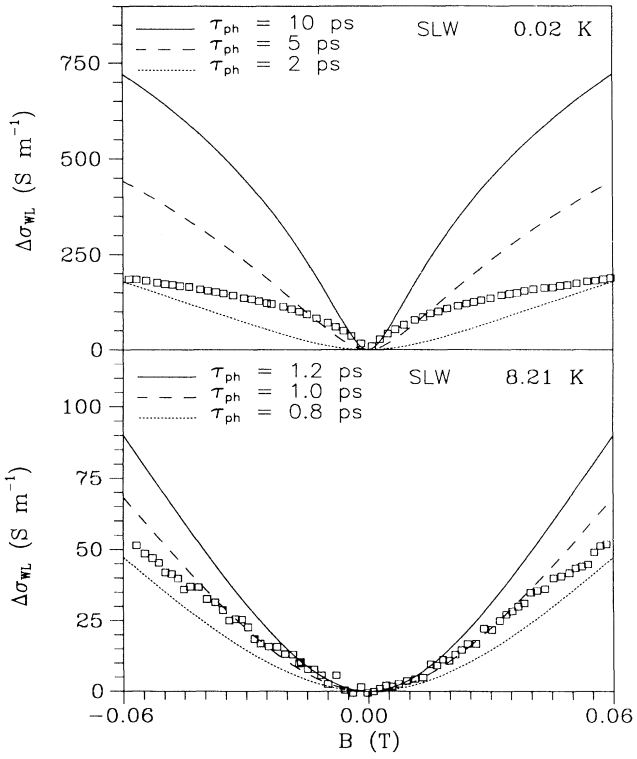

FIG. 6. Data vs 2D theory of weak-localization corrections to magnetoconductivity in SLW at two different temperatures. Results are analogous to those for SLN shown in Fig. 5.

$\sigma_{WL}(B) - \sigma_{WL}(0)$, obtained from Eq. (15). Here, the classical resistivity ρ_{xx}^{cl} was 4.762 (7.692) $\times 10^{-5}$ Ω m.

For comparison, the same figures present theoretical predictions calculated according to Eq. (13) and normalized per one superlattice period. The theoretical curves in each plot are drawn for three different dephasing times, τ_{ph}. All other parameters entering Eq. (13) were determined earlier. The discrepancy between theory and experiment is especially obvious at low temperatures. The theoretical curves fitting the experimental points at very small fields significantly overestimate the effect at higher fields with the difference increasing with B. By introducing a phenomenological prefactor $\alpha < 1$ into the theoretical formula of Eq. (13) one can reduce $\Delta\sigma_{WL}^{2D}$ and make the theory comparable to the experiment results. Because of the normalization condition for $\Delta\sigma_{WL}$, the prefactor α would be equivalent to the fraction $\frac{N_{eff}}{N}$, where N_{eff} and N are the effective and real number of layers, respectively. The values of α determined in such a procedure vary between ≈ 0.45 for low temperature ($T < 0.1$ K) and ≈ 0.60 for high temperature ($T > 1$ K) in SLN, and between ≈ 0.14 for $T < 1$ K and ≈ 0.30 for $T > 8$ K in SLW. We rule out the justification of these small prefactors as coming from the reduction of the number of effective 2D layers (wells). The known geometry of the samples cannot be reconciled with the small prefactors even in the presence of the depletion of a few top and bottom layers due to the pinning of the Fermi level caused by the deep Cr^+ impurity levels in the substrate and by midgap surface states at the cap layer.[12]

The same problem appeared in previous work on positive magnetoconductivity (caused by antilocalization effects from dominant spin-orbit scattering) by Moyle, Cheung, and Ong,[33] who obtained $\alpha = 0.3 - 0.42$ in HgTe/CdTe superlattices treated as 2D systems. Also, magnetotransport studies[37] of 2D Si MOSFET's revealed the necessity of introducing an analogous prefactor $\alpha \approx 0.3$. However, as proved by Fukuyama[38,39] that prefactor took into account an intervalley scattering effect. This effect is absent in GaAs-based systems due to its simple band structure. In GaAs/Al_xGa_{1-x}As heterostructures[28] the prefactor α was found to be greater than 0.75 and was ascribed to superconducting fluctuation effects. However, the same samples also revealed logarithmic changes in conductivity with temperature which are characteristic of 2D systems.

In our case, α is significantly smaller than 0.75. It also changes with temperature—an effect not observed in GaAs/Al_xGa_{1-x}As heterostructures.[28] In addition, the large difference (by a factor of 2) in α between

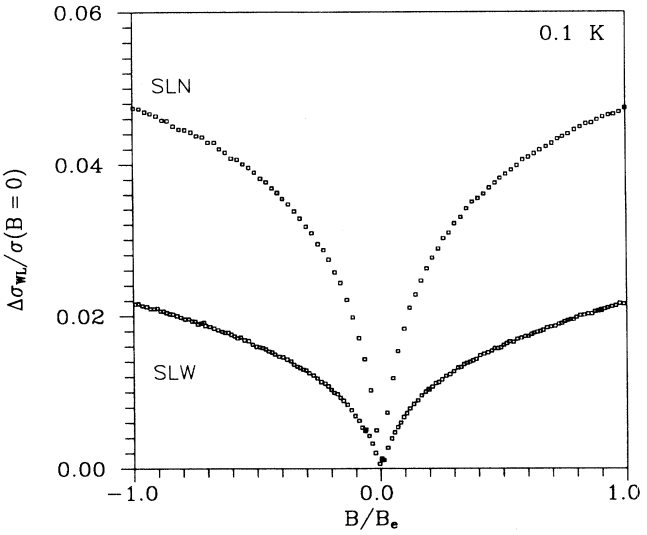

FIG. 7. Comparison of weak-localization corrections to magnetoconductivity in SLN and SLW. Experimental results are presented in reduced form, $\Delta\sigma_{\rm WL}/\sigma(B=0)$ vs B/B_e. The total zero-field conductivity is $\sigma(B=0)$, and B_e is the characteristic field for elastic scattering.

the two superlattices strongly suggests that the anomalous magnetoconductivity is sensitive to those parameters of the superlattices which are neglected in the 2D approach, i.e., parameters describing interlayer coupling. Indeed, smaller values of α were found in SLW which is characterized by lower potential barriers and, therefore, stronger interlayer coupling. Consequently, this sample is more "three dimensional" than the other superlattice with higher potential barriers. This argument is logically consistent with the well-known fact of decreasing weak-localization effects with the increasing effective dimensionality of a system.

Experimental confirmation of the conclusion reached above is shown explicitly in Fig. 7 where the magnetoconductivity data are plotted in a reduced form $\Delta\sigma_{\rm WL}/\sigma(B=0)$ as a function of the reduced magnetic field B/B_e for the two superlattices at the same temperature. Here, the use of reduced quantities eliminates the difference in classical transport parameters (v_F, τ_e). This figure clearly illustrates the correlation between the superlattice structure and the magnitude of the weak-localization corrections to magnetoconductivity.

C. Weak localization: Analysis with superlattice-specific models

The failure of the 2D weak-localization theory to satisfactorily explain the positive magnetoconductivity in superlattices calls for the use of other theoretical models that adequately take into account the intrinsic properties of these periodic structures. Such theoretical models of weak-localization effects specific to superlattices were developed in Refs. 14–16. The basic model (Ref. 14) introduced the main feature of weak localization in superlattices, namely its transitional character between bulk 2D and 3D versions of this phenomenon. However, this model is restricted to low magnetic fields. In addition, it does not allow for subtle effects of electron wave-function modulation and impurity distribution. A direct application of this model to study experimental results, which were published elsewhere,[40] required introducing a phenomenological parameter into the magnetoconductivity formula in order to account for the experimental results at higher magnetic fields. Also, the vertical diffusion constant derived from the data was different from the theoretically predicted value by $\approx 50\%$. Therefore, the basic model was subsequently improved in a twofold manner. One improvement led to the structure dependent model (Ref. 15) where the electron wave-function modulation and a nonuniform impurity distribution were taken into account. The main result of this model can be described as a renormalization of the diffusion tensor. The other model (Ref. 16) elaborates on high magnetic-field effects. Due to relatively large mobilities of the samples, the characteristic fields (B_e, $B_{\rm ph}$) are very small. Consequently, the magnetic field which would normally be considered quite weak (≈ 0.1 T) becomes large with respect to weak-localization effects. In addition, measurements at very low fields are restricted by the resolution (≈ 1 mT) of the experimental setup. On the other hand, results at higher fields show more complicated and also more sample-specific features than those at low fields which become a quadratic function of the magnetic field ($\Delta\sigma_{\rm WL} \propto B^2$ for $B \to 0$). This conclusion can be inferred from Eqs. (34) and (36) of Ref. 14, and from the asymptotic form of the Kawabata function [Eq. (35) of Ref. 14]. In the following analysis of the experimental data, the high-field model will be used and the superlattice structure effects discussed above will be included through the renormalized diffusion constants.

The procedure of fitting theoretical curves to the experimental data involves a numerical integration step in the expression for $\Delta\sigma_{\rm WL}(B)$, (see Ref. 16), namely

$$\Delta\sigma_{\parallel,\rm WL}(B) = -\frac{2e^2 D_\parallel \tau_e}{\pi\hbar}\frac{eB}{\pi\hbar}\sum_n \int \frac{dq_z}{2\pi}\left[Q(n,q_z) - \int_n^{n+1} dn' Q_0(n',q_z)\right]. \tag{16}$$

Intermediate steps require calculations of the Cooperon-related functions Q and Q_0 defined as

$$Q(n,q_z) = \left[1 - \frac{\tau}{\tau_e}\int_0^\infty dx\, e^{-\frac{\alpha}{2}x^2 - x} L_n(\alpha x^2) J_0(\beta x)\right]^{-1}, \tag{17}$$

and

$$Q_0(n,q_z) = \left[1 - \frac{\tau}{\tau_e}\frac{F(\frac{3}{4},\frac{1}{4};1;y^2)}{\sqrt{1+4(n+\frac{1}{2})\alpha+\beta^2}}\right]^{-1}, \tag{18}$$

where L_n is the Laguerre polynomial of the nth order, J_0 is the zeroth-order Bessel function, F is the hypergeometric function,

$$y = \frac{4\beta\sqrt{(n+\frac{1}{2})\alpha}}{1+4(n+\frac{1}{2})\alpha+\beta^2}, \tag{19}$$

$$\alpha = \frac{2eD_{\|}\tau^2}{\hbar\tau_e}B = \frac{1}{2}\frac{B}{B_e}\left(\frac{\tau}{\tau_e}\right)^2, \tag{20}$$

$$\beta = \sqrt{\frac{2D_z\tau^2}{\tau_e}}\frac{\sin(\frac{1}{2}q_z a)}{\frac{1}{2}a}, \tag{21}$$

and

$$\frac{1}{\tau} = \frac{1}{\tau_e} + \frac{1}{\tau_{\rm ph}} \tag{22}$$

is the total scattering rate involving the dephasing time $\tau_{\rm ph}$. (To abbreviate the notation, we use here Q and Q_0 instead of the Cooperon functions Π and Π_0 referred to in Ref. 16. They are related through $Q = [1 - n_{\rm imp}V^2\Pi]^{-1}$ and an analog expression for Q_0.) The parallel diffusion constant $D_{\|}$ is determined from the measured mobility and density of carriers according to the standard expression,

$$D_{\|} = \left\langle \frac{\mathbf{v}_{\|}^2\tau}{2} \right\rangle_{FS} \approx \frac{\varepsilon_F\tau_e}{m^\star}, \tag{23}$$

where the Fermi energy ε_F is large compared to the superlattice miniband width $2w$. $D_{\|}$ does not depend explicitly on the details of the superlattice structure and impurity profile. Such a dependence does exist for the vertical diffusion constant D_z, as calculated in Ref. 15, viz., $D_z = D_{z,c} + D_{z,h}$, where

$$D_{z,c} = \langle v_z^2\tau\rangle_{FS} = \frac{w^2a^2\tau_e}{\hbar^2}\frac{\sqrt{1-b^2}}{1+\sqrt{1-b^2}} \tag{24}$$

is the coherent term, and

$$D_{z,h} = \frac{a^2}{2\tau_e}\frac{1}{\sqrt{1-b^2}}\frac{P_{n,n\pm1}}{P_{n,n}+P_{n,n\pm1}} \tag{25}$$

is the hopping diffusion term. Here, the parameter b describes the scattering anisotropy, and $P_{n,n\pm1}/[P_{n,n} + P_{n,n\pm1}]$ is the relative interlayer hopping probability (probabilities $P_{n,n}$ and $P_{n,n\pm1}$ are defined in Ref. 15). They depend explicitly on electron wave-function modulation and the impurity distribution. We use the known superlattice parameters (w, a, τ_e) and calculate b and $P_{n,n\pm1}/(P_{n,n} + P_{n,n\pm1})$ for three different scattering cases:[15] (a) impurities (dopants) confined to the barrier regions, (b) impurities located at interfaces, and (c) impurities uniformly distributed throughout the superlattice layer structure. These values are then used to obtain the vertical diffusion constant. The results are shown in Table II.

Given the diffusion constants ($D_{\|}$, D_z), scattering time (τ_e), and the superlattice constant (a), the Cooperon-related functions (Q and Q_0) and, subsequently, the magnetoconductivity are calculated as a function of magnetic field B with the dephasing time $\tau_{\rm ph}$ being the *only* adjustable parameter. The results of these calculations are then compared with the experimental data. Typical plots of this comparison are shown in Figs. 8 and 9 for low- and high-temperature regimes in SLN and SLW, respectively. Both cases of the nonuniform impurity distribution underestimate the magnetoconductivity effect. (Here, $\tau_{\rm ph}$ was adjusted in attempts to reproduce data at least in small fields.) The difference between the theory and experiment becomes particularly large at low temperatures. For example, in the case of the in-barrier scattering in SLN at $T = 0.025$ K even extremely large dephasing times $\tau_{\rm ph} \approx 10^5$ ps result in the magnetoconductivity being smaller than the measured one by a factor of ≈ 2. This difference decreases with temperature; nevertheless, the overall tendency is preserved. On the contrary, the experimental results are quite consistent with a uniform distribution of scattering centers throughout the superlattice structure. A small deviation from uniformity may occur in SLN, but it cannot be ascribed decisively to a particular distribution case. For the case of the uniform impurity distribution, the results of the one-parameter fitting procedure over the full temperature range are shown by the solid curves through the data in Figs. 10 and 11 for SLN and SLW, respectively.

A general comment about this comparison between theory and experiment is that the theoretical model of weak localization with an effective uniform distribution of impurities reproduces the magnetoconductivity data very well. This agreement is remarkable in SLW where it holds through *three* decades of temperature changes ($T = 0.02$–19.2 K) and persists up to a magnetic field of 0.06 T ($\approx 0.5B_e$). In the case of SLN, the theory

TABLE II. Effect of impurity distributions on superlattice parameters.

Superlattice	Impurity distribution	b	$\frac{P_{n,n\pm1}}{P_{n,n\pm1}+P_{n,n}}$	D_z $(\mathrm{cm^2\,s^{-1}})$
SLN	uniform	0.0018	3.3×10^{-5}	0.42
	interface	0.17	0.015	0.59
	in-barrier	0.32	0.070	1.2
SLW	uniform	0.031	2.1×10^{-3}	4.6
	interface	0.48	0.012	6.1
	in-barrier	0.71	0.27	8.9

works very well at fields $B \leq 0.03$ T ($B \leq 0.4B_e$). A small deviation from the data is seen at low temperatures ($T \leq 0.1$ K) and $B \geq 0.02$ T as pointed out above. This conclusion is not expected in view of the known parameters of the superlattices. Both superlattices were selectively doped in narrow layers at the centers of the barrier regions. However, silicon dopant migration during MBE growth has recently been found to be an important process.[3–6] On the other hand, there is evidence suggesting that we should not think of this happening to the extent that dopant atoms are completely and uniformly spread throughout the whole superlattice. A second source for the apparent agreement between the data and a theoretical model of weak localization with an effective uniform distribution of impurities is that the actual scattering from ionized dopants of a sharply defined distribution can be thought of as mimicking the scattering from point impurities of a broader distribution. From this viewpoint the ionized dopants in the barriers

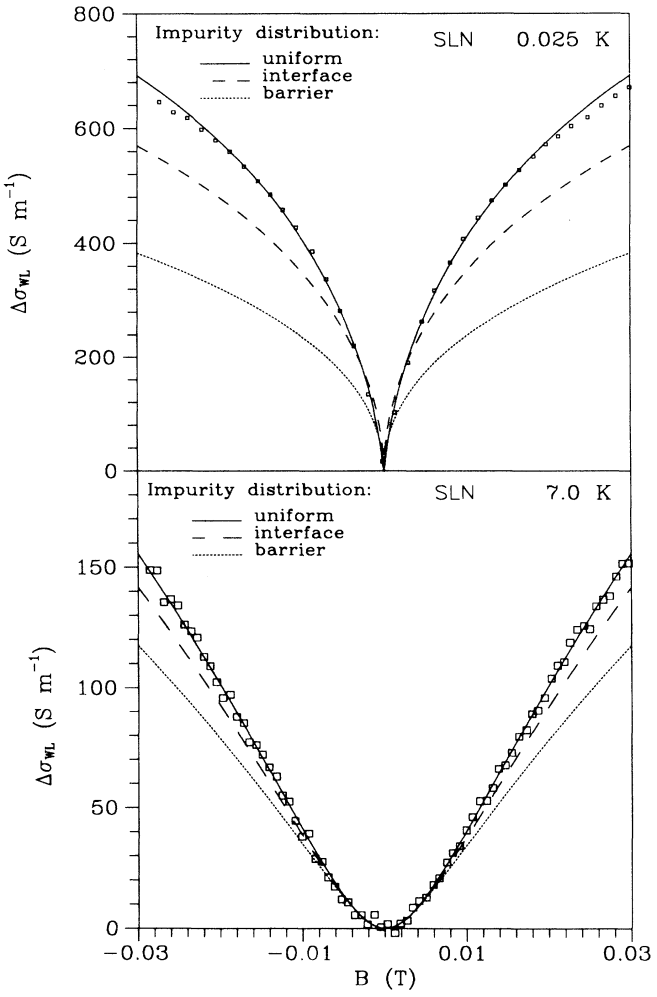

FIG. 8. Weak-localization corrections to magnetoconductivity in SLN at two different temperatures. Squares represent experimental points. Curves are theoretical results for three different impurity distributions.

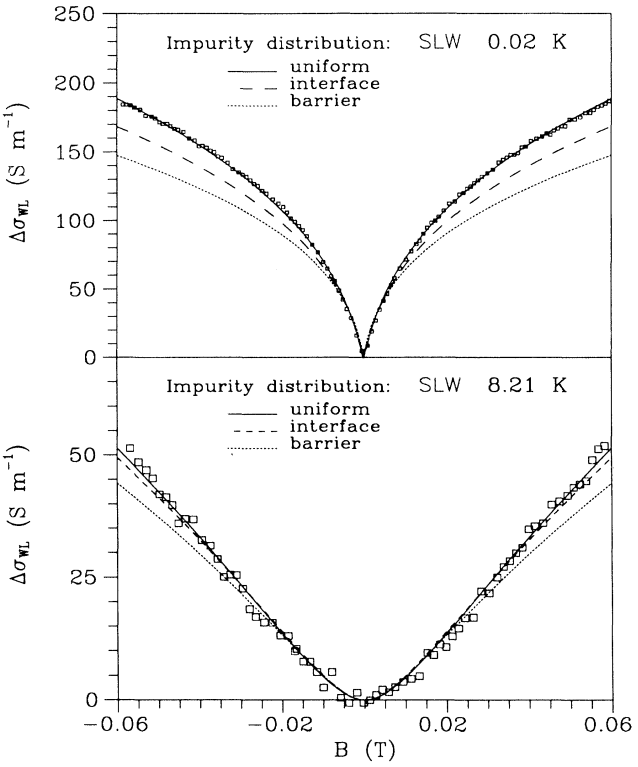

FIG. 9. As in Fig. 8 for SLW.

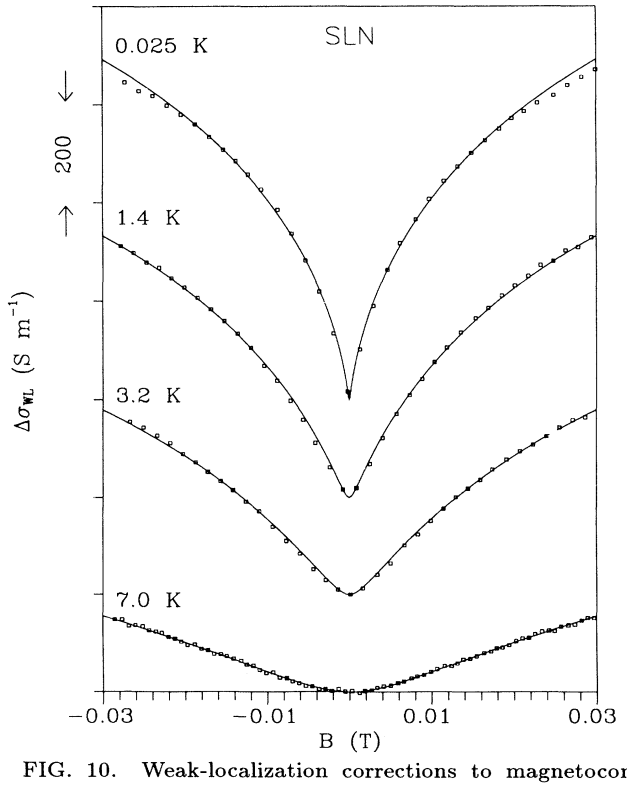

FIG. 10. Weak-localization corrections to magnetoconductivity in SLN at various temperatures. Curves through the points are *one-parameter* fits of the weak-localization theory in superlattices (the case of uniform impurity distribution). Note that the data have been vertically offset for viewing.

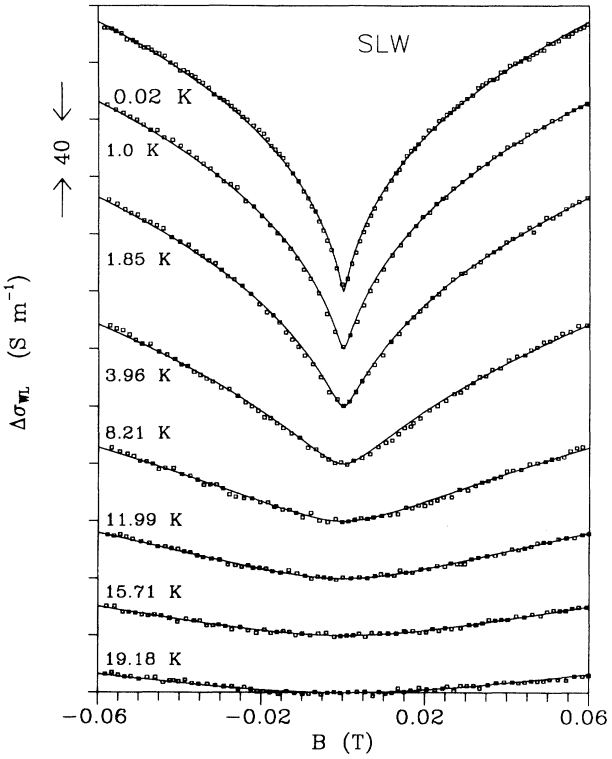

FIG. 11. As in Fig. 10 for SLW. Note the agreement through three decades of temperature up to $\frac{1}{2}B_e$ in magnetic field.

are not effectively screened by the electron gas of the reduced local density; therefore the electrons are scattered by slowly decaying Coulomb potentials at distances significantly larger than those implied by simple geometrical arguments as applied to sharply defined doping profiles.

To provide a more convincing argument of this point, let us examine an example of an extremely localized impurity distribution described by a δ function at the barrier centers. The scattering potential is assumed to be separable with respect to the space coordinates, i.e., $V_i(\mathbf{r}_{\|}, z) = V_{\|}(\mathbf{r}_{\|} - \mathbf{R}_i)V_z(z - Z_i)$, where $(\mathbf{R}_i, Z_i)$ are the impurity coordinates. Here the parallel component $V_{\|}$ is neglected for simplicity, and V_z takes the steplike form $V_z(z - Z_i) = V\theta(\frac{r}{2} - |z - Z_i|)$, where $\frac{r}{2}$ is the potential range. Details of these calculations are presented in the Appendix of Ref. 15. The result for the scattering anisotropy factor b is given by Eq. (A14), viz., $b = \beta r/\sinh(\beta r)$, where β is a parameter that describes the electron wave function in the barriers. The potential range $\frac{r}{2}$ is taken to be the screening length $\lambda_s = 7.6$ nm which was calculated using the standard formula for a degenerate electron gas, $\lambda_s^2 = e^{-2}\varepsilon_0\varepsilon g^{-1}(\epsilon_F)$, where $\varepsilon = 12.9$ is the dielectric constant of GaAs. The substitution of realistic parameters for a superlattice (e.g., sample SLW) yields $b \approx 0.4$. This value should be compared to $b = 1$ calculated for a short-range (pointlike) potential. Obviously, the finite range of the scattering potential affects the b factor in a way similar to what a short-range (pointlike) potential does in the case of a more uniform distribution.

A more exact treatment of this aspect of weak-localization effects requires a new theory not limited by the simplified assumption of short-range scattering but rather using the more realistic screened Coulomb interactions. This refers not only to superlattice structures but also, more generally, to all semiconductor systems where ionized impurities play a dominant role in the transport properties. At this time such a theory does not exist mainly due to its evident complexity.

D. Dephasing time

The theoretical analysis of the magnetoconductivity data presented in the previous section allows us to determine the dephasing time $\tau_{\rm ph}$. This parameter is shown as a function of temperature in Figs. 12 and 13 for SLN and SLW, respectively. It was found from fitting the weak-localization theory for the uniform impurity distribution to the data (Figs. 10 and 11). Both superlattices reveal very similar behavior for $\tau_{\rm ph}$. There exist two temperature regions (above and below ≈ 0.5 K), where the dephasing time shows a different temperature dependence. In both regions a single-term power function $\tau_{\rm ph} = CT^{-p}$ was fitted to the experimental results. At temperatures above 0.5 K the dephasing time obeys the power law with $p = 1.52$ (1.45) and $C = 93.2$ (91.2) ps K^p. In the other region ($T \leq 0.5$ K) $\tau_{\rm ph}$ is almost temperature independent. The exponent p is very close to zero [$p = 0.01$ (0.02)] and the constant C amounts to 271 (209) ps K^p.

The dephasing time is an important parameter in weak-localization theories. It sets an upper scale for the quantum interference phenomena (a lower one is given by the elastic-scattering time). As pointed out by Altshuler and Aronov[41] this phase relaxation time is the shortest observable energy relaxation time in a system.

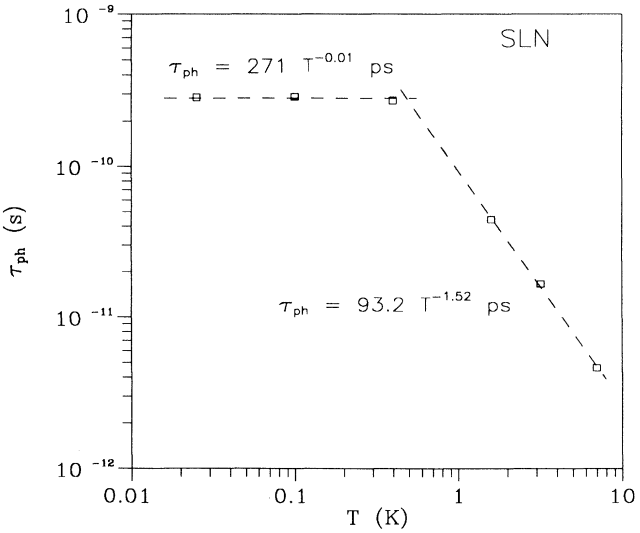

FIG. 12. Dephasing time $\tau_{\rm ph}$ as a function of temperature T in SLN. Squares represent results of magnetoconductivity fits in Fig. 10. Dashed lines are power-law fits to the data.

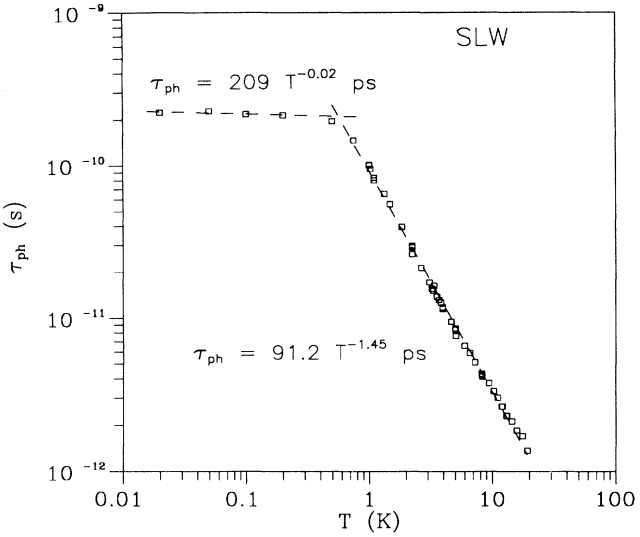

FIG. 13. As in Fig. 12 for SLW. Squares represent results of magnetoconductivity fits in Fig. 11.

High-temperature region. In a majority of weakly disordered systems at low temperatures, the electron-phonon scattering becomes negligible and inelastic electron-electron collisions with the rate $\tau_{e\text{-}e}^{-1}$ are the dominant processes which determine the energy relaxation time. Altshuler, Aronov, and Khmel'nitskii[42] showed that in 3D the phase relaxation time is governed by processes with large energy transfer ($\Delta\epsilon \approx kT$) for which the equality $\tau_{ph} \approx \tau_{e\text{-}e}$ holds. In 3D isotropic systems, collisions with small momentum transfer $q \ll q_s$ (where q_s is an inverse screening length) contribute to the electron-electron scattering rate[43] as a term proportional to $T^{3/2}$,

$$\frac{1}{\tau_{e\text{-}e,S}} \propto \frac{g'}{\hbar g(\epsilon_F)} \left(\frac{kT}{\hbar D}\right)^{3/2}, \tag{26}$$

where g' is a dimensionless coupling constant, $g(\epsilon_F)$ is the density of state at the Fermi energy ϵ_F, and D is an isotropic diffusion constant. Processes with a large momentum transfer yield a scattering rate proportional to T^2, i.e.,

$$\frac{1}{\tau_{e\text{-}e,L}} \propto \frac{(kT)^2}{\hbar\epsilon_F} \frac{q_s}{p_F}, \tag{27}$$

where p_F is the Fermi momentum. These collisions are characteristic of pure systems where the scattering rate is determined by the available phase space and does not depend on the details of the electron-electron interaction. In general, both processes should be taken into account and the resultant scattering rate acquires the form

$$\frac{1}{\tau_{e\text{-}e}} = C_1 T^{3/2} + C_2 T^2. \tag{28}$$

However, in the special case of weak screening where $q_s \leq p_F$ the contribution from large momentum transfer becomes small and

$$\frac{1}{\tau_{e\text{-}e}} = C_1 T^{3/2} \tag{29}$$

is a very good approximation.

The temperature behavior of τ_{ph} found for the superlattices in the high-temperature region satisfies this relation extremely well. A rough estimate of the scattering rates for the small and large momentum transfer collisions shows that, indeed, the former exceeds the latter by at least one order of magnitude in the superlattices where $q_s \approx p_F$ holds.

A detailed quantitative analysis of τ_{ph} requires a theory of electron-electron interaction effects in superlattices. Such a theory does not exist at this time. In order to make an approximate estimate of the electron-electron scattering time, the expression of Eq. (26) is modified to include anisotropy of a superlattice by the replacement $D^3 \to D_{||}^2 D_z$, which yields

$$\frac{1}{\tau_{e\text{-}e}} \propto \frac{g'}{\hbar g_{SL}(\epsilon_F)} \sqrt{\frac{(kT)^3}{\hbar^3 D_{||}^2 D_z}}. \tag{30}$$

This expression results in $\tau_{e\text{-}e} = 11\ (25)\ \mathrm{T}^{-3/2}\,\mathrm{ps\,K}^{3/2}$. Here, the following values of the involved parameters were used: $g' = 1$, $g_{SL}(\epsilon_F) = 7.69 \times 10^{43}\ \mathrm{J^{-1}\,m^{-3}}$, $D_{||} = 1.0 \times 10^{-2}(0.69 \times 10^{-2})\ \mathrm{m^2\,s^{-1}}$, $D_z = 4.2 \times 10^{-5}(4.6 \times 10^{-4})\ \mathrm{m^2\,s^{-1}}$.

The results obtained from the experiment, i.e., $\tau_{e\text{-}e} = 93.2\ \mathrm{T}^{-1.52}\,\mathrm{ps\,K}^{1.52}$ ($91.2\ \mathrm{T}^{-1.44}\,\mathrm{ps\,K}^{1.44}$) show an order-of-magnitude agreement with the values calculated above. The lack of any difference in $\tau_{e\text{-}e}$ between the two superlattices is not confirmed by these rough calculations and clearly requires a more detailed theoretical model.

Low-temperature region. In this region the dephasing time is practically temperature independent and the corresponding dephasing length in the direction parallel to the superlattice layered structure is calculated to be $\ell_{ph} = \sqrt{D_{||}\tau_{ph}} = 1.67\ (1.23)\ \mu$m. A very abrupt onset of the temperature-independent dephasing time (particularly obvious in SLW) strongly suggests an electron heating effect. The absence of a T^{-3} term in the dephasing time (this temperature dependence is characteristic of the electron-phonon scattering) and the dominant contribution of electron-electron collisions to inelastic processes imply that electrons can redistribute energy among themselves but there is no effective channel for energy loss. Thus, the electron heating effect results from the fact that the phonon relaxation time for electrons becomes so long that the electron gas, having absorbed excess energy, cannot cool down to the lattice temperature in the finite size of the sample. This effect can be studied quantitatively using a simple two-bath model.[44]

Using this model we obtain the following electron-phonon scattering rate (for SLN)

$$\frac{1}{\tau_{e\text{-}p}} = 4.1 \times 10^6\ \mathrm{T}^3\ \frac{1}{\mathrm{s\,K^3}}.$$

This result implies very large relaxation lengths at low temperature, e.g., at T= 0.1 K $l_{e\text{-}p} = \sqrt{D_{||}\tau_{e\text{-}p}} =$

1.5 mm. It is also consistent with the high-temperature behavior of $\tau_{\rm ph}$. At $T = 20$ K $\tau_{e\text{-}p} = 30$ ps which is significantly greater than $\tau_{e\text{-}e} = 1.0$ ps; thus the dephasing time $\tau_{\rm ph} = \tau_{e\text{-}e}$ to a very good accuracy.

Wennberg and co-workers[44] studied the electron-energy-loss rate in n-doped GaAs/$Al_xGa_{1-x}As$ heterostructures with lateral sizes 6×6 mm and equivalent 3D density of carriers $n = 2.7 \times 10^{22}$ m^{-3}. They found the electron-phonon scattering rate to be

$$\frac{1}{\tau_{e\text{-}p}} = 2.5 \times 10^6 \ \mathrm{T}^3 \ \frac{1}{s\,\mathrm{K}^3}.$$

In another experiment Roukes *et al.*[45] measured the energy relaxation rate in a metal (Cu) film which had dimensions 6 cm$\times$10 μm$\times$100 nm. They also found $p = 3$ and their corresponding relaxation rate was

$$\frac{1}{\tau_{e\text{-}p}} = 9 \times 10^7 \ \mathrm{T}^3 \ \frac{1}{\mathrm{s\,K}^3}.$$

Consequently, the electron-phonon scattering rate found in our superlattice is consistent with the analogous parameters obtained in other systems. This allows us to consider the electron heating effect as the probable cause for saturation of the dephasing time at low temperatures.

V. ZERO-FIELD CONDUCTIVITY

Results of the zero-field conductivity measurements are shown in Figs. 14 and 15 where the temperature changes of $\sigma(T)$ relative to the low-temperature limit $\sigma(T \to 0)$ are plotted versus temperature.

In the regime of very low temperatures, the conductivity becomes temperature-independent. This is consistent with the behavior of the magnetoconductivity discussed earlier and quantitatively described in terms of the dephasing time. However, in the case of the zero-field conductivity, the transition region leading to the temperature-independent regime is broader and the latter begins at lower temperatures ($T \approx 0.2$–0.3 K instead of $T = 0.5$ K). Above the transition region the two superlattices reveal a qualitatively different temperature dependence of $\sigma(T)$. In SLN, the conductivity $\sigma(T)$ is approximately linear in temperature while SLW displays more parabolic-type behavior, suggesting a larger contribution from the semiclassical effect. As in the case of the Hall factor r_H discussed in Sec. III, the semiclassical corrections at low temperature ($T \ll T_F$) are quadratic in T

$$\delta\sigma_{\rm cl}(T) = \sigma_{\rm cl}(T) - \sigma_{\rm cl}(0) = \sigma_{\rm cl}(0)\frac{\pi^2}{6}\eta(\eta+1)\left(\frac{T}{T_F}\right)^2, \tag{31}$$

where η is the energy exponent introduced in Sec. III. Using the value of η determined from the temperature dependence of the Hall constant [$\eta = 2.2$ (1.3)], the Fermi temperature $T_F = 198$ (160) K, and approximate numbers for the classical term of the conductivity at $T = 0$, $\sigma_{\rm cl}(0) = 20\,700$ (12 071) S m^{-1} consistent with the values used earlier in the magnetoconductivity analysis, the semiclassical contribution is calculated and the results are plotted as dashed curves in Figs. 14 and 15. It should be noted here that $\sigma_{\rm cl}(0)$ cannot be determined directly from the experiment. The estimates used are subject to an error (of a few percent) which prevents us from calculating the absolute values of $\sigma_{\rm cl}(T)$ with sufficient accuracy to make comparison with data. However, the temperature changes $\delta\sigma_{\rm cl}(T)$ do not suffer from this disadvantage and a few percent accuracy is sufficient to make reliable analysis. As seen in Fig. 15, the semiclassical effect contributes significantly ($\approx 70\%$) to the observed

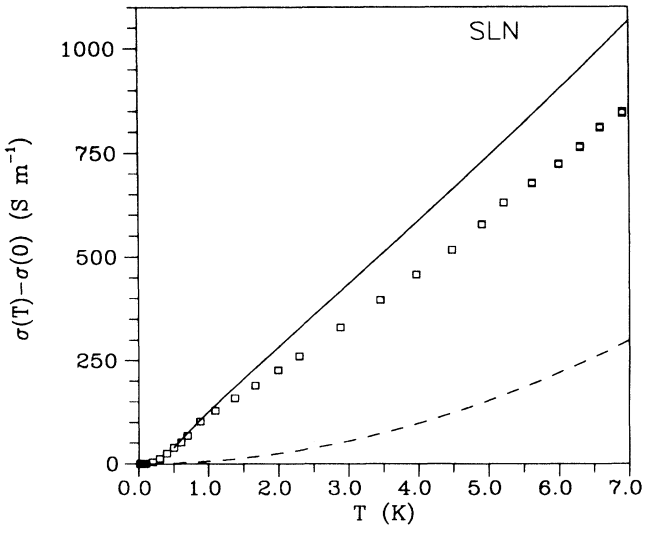

FIG. 14. Zero-field conductivity as a function of temperature in SLN. Squares represent experimental data. The dashed curve gives the values of semiclassical corrections. The solid curve includes both semiclassical and weak-localization corrections with *no* adjustable parameters.

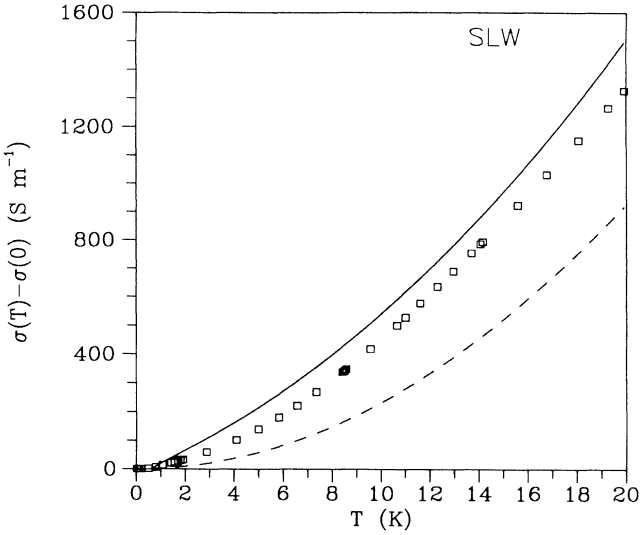

FIG. 15. As in Fig. 14 for SLW.

changes of $\sigma(T)$ in SLW and determines the quadratic-T form. On the other hand, this same effect gives only 35% of the total conductivity increase in SLN (see Fig. 14).

Next, the weak-localization contribution[16] $\delta\sigma_{\|,\mathrm{WL}}(T, T_0)$, describing the change of the conductivity between temperatures T and T_0

$$\delta\sigma_{\|,\mathrm{WL}}(T,T_0) \equiv \sigma_{\|,\mathrm{WL}}(T) - \sigma_{\|,\mathrm{WL}}(T_0). \tag{32}$$

is calculated according to

$$\delta\sigma_{\|,\mathrm{WL}}(T,T_0) = -\frac{2e^2 D_\| \tau_e}{\pi\hbar}\int\frac{d^2q_\|}{4\pi}\int\frac{dq_z}{2\pi}[Q_{00}(q_\|,q_z,\tau(T)) - Q_{00}(q_\|,q_z,\tau(T_0))], \tag{33}$$

where

$$Q_{00}(q_\|,q_z,\tau(T)) = \left[1 - \frac{\tau}{\tau_e}\frac{F(\frac{3}{4},\frac{1}{4};1;y_0^2)}{\sqrt{1+\frac{2D_\|\tau^2}{\tau_e}q_\|^2+\beta^2}}\right]^{-1}, \tag{34}$$

$$y_0 = \frac{2\beta\sqrt{\frac{2D_\|\tau^2}{\tau_e}}q_\|}{1+\frac{2D_\|\tau^2}{\tau_e}q_\|^2+\beta^2}, \tag{35}$$

and other quantities were defined in Sec. IV C. The reference temperature T_0 was fixed in the low temperature range (T_0 = 0.5 K) above the onset of the apparent self-heating effects. It should be emphasized that all parameters used in this calculation were determined earlier from (i) the superlattice structure (superlattice period, miniband width), (ii) the basic transport properties of the samples (mobility, density of carriers), and (iii) the magnetoconductivity fits (dephasing time). Hence, *no free* parameters are used here to adjust the results to the data. These results are determined for temperatures above 0.5 K where the heating effect is absent. They are combined with $\delta\sigma_{\mathrm{cl}}(T)$ and plotted as solid lines in Figs. 14 and 15. The theoretical results correctly reproduce the general trend in the temperature dependence of $\sigma(T)$ but slightly overestimate their magnitude. In the case of SLN the linearity of $\sigma(T)$ is confirmed by the theory but the theoretical slope is $\approx$ 25% larger than the observed one. In SLW the rate of the temperature change in $\sigma(T)$ is correctly increased from that implied by the semiclassical theory and the parabolic shape is retained. The difference between the theoretical values and experimental results amount to 13% at a maximum temperature of T = 20 K.

There are a few possible reasons for this modest disagreement between the experiment and theory. The parameter η as obtained from the data (the Hall constant in the zero-field limit) carries large errors, especially in SLN (see Fig. 3), and is the least accurate parameter (with an error of up to 10%).

It is worth noticing that for a difference between the theory and experiment which amounts to 13% (25%) of the temperature changes, $\delta\sigma$ corresponds to merely 1% of the absolute value of the conductivity. There is a whole group of classical effects which reduce conductivity at finite temperatures but they are small and usually neglected in the temperature regime of interest. An example is given by the electron-phonon scattering. This process makes the total scattering time τ (and also the momentum relaxation time) a weakly decreasing function of temperature. Using the standard Drude formula this effect may be estimated by

$$\frac{\delta\sigma}{\sigma} = \frac{\tau}{\tau_{e\text{-}p}}. \tag{36}$$

Now substituting realistic values of τ = 0.2 ps and $\tau_{e\text{-}p}$ = 30 ps (found in Sec. IV D at T = 20 K) yields

$$\frac{\delta\sigma}{\sigma} = 0.67\%,$$

which is of the same order of magnitude as the difference under consideration.

It should be emphasized that the data does not show a logarithmic temperature dependence for $\sigma(T)$ typical of 2D weakly localized systems. In addition, it may be shown that a 2D analysis is subject to the following inconsistency. From the best 2D fits to the magnetoconductivity data (including prefactor α, see Sec. IV B) τ_{ph} was found to be 52.8 ps at T = 0.1 K and 3.7 ps at T = 7.0 K in SLN, and 36.3 ps at T = 0.02 K and 1.02 ps at T = 19.2 K in SLW. Applying the standard formula for 2D weak-localization corrections to the conductivity (normalized per one layer)

$$\delta\sigma_{\mathrm{WL}}^{\mathrm{2D}}(T_1,T_2) = \sigma_{\mathrm{WL}}^{\mathrm{2D}}(T_1) - \sigma_{\mathrm{WL}}^{\mathrm{2D}}(T_2) = \frac{e^2}{2\pi^2\hbar a}\ln\left[\frac{\tau_{\mathrm{ph}}(T_2)}{\tau_{\mathrm{ph}}(T_1)}\right], \tag{37}$$

yields

$$\delta\sigma_{\mathrm{WL}}^{\mathrm{2D}}(7\ \mathrm{K}, 0.1\ \mathrm{K}) = 1450\ \mathrm{S\,m^{-1}}$$

for SLN, and

$$\delta\sigma_{\mathrm{WL}}^{\mathrm{2D}}(19.18\ \mathrm{K}, 0.02\ \mathrm{K}) = 1950\ \mathrm{S\,m^{-1}}$$

for SLW.

These results are significantly larger (by more than 50%) than the measured $\delta\sigma$ even with the semiclassical term excluded. Consequently, the 2D weak-localization theory cannot account for the temperature changes in the zero-field conductivity observed in the superlattices.

VI. CONCLUSIONS

We believe future progress in the area of weak-localization is related to studying systems for which more

detailed microscopic information is available. Specifically, we have studied superlattices with controlled impurity distributions. In previous measurements[2,27] on 2D and 3D systems, only uniform impurity cases were studied, which obscured finite-range-potential effects. For example, in a standard heterojunction geometry, the electron sees only small variations in the ionized dopant potential because of averaging effects from a dopant distribution that is remote and uniform throughout a plane. On the other hand, in superlattices, the electron, due to its coherent vertical motion, probes all distances of an ionized impurity potential. Consequently, superlattice structures are well suited for probing more deeply these types of quantum interference transport mechanisms.

We measured the parallel magnetotransport properties of two $GaAs/Al_xGa_{1-x}As$ superlattices with identical impurity profiles but with a different alloy composition of $Al_xGa_{1-x}As$. We found that the zero-field conductivity did not display a logarithmic temperature dependence as characteristic of quasi-two-dimensional systems; instead a weaker power-law dependence which is typical of 3D structures was found. Similarly, the magnetoconductivity data could not be explained by the 2D WL theory. Consequently, to quantitatively analyze the experimental results we used a recent theory that incorporates the superlattice structure in the z direction, including impurity profile and electron wave-function modulation. Therefore, we are able to adequately describe the bandwidth dependence on quantum corrections to the conductivity. This theory, however, still assumes a pointlike scattering potential model. We then compared the experimental magnetoconductivities with theoretical ones calculated for various impurity profiles. As a result, we found that although the samples were intentionally doped in the barrier regions, the best fits were obtained using a uniform impurity profile model.

We can explain these results in two ways: (i) the data show the influence of the long-range potential on weak-localization effects; (ii) the best fit is obtained using a pointlike scattering model compatible with the experimental data provided that the real dopant distribution is different from the nominal one (as intended by the grower). Here one has to assume that silicon migration during growth is the reason the dopant spreads out of the barriers where it was originally placed. Evidence for silicon migration has been recently reported,[3–6] and since the barriers in our samples are thin we expect this effect to be operative but not dominant.

Further progress towards a fully realistic description of WL will be difficult when applied to the superlattice structures used in this study. First, if the real impurity profile is properly accounted for, then the difference in contributions from long-range scattering compared to effective pointlike scattering will be smaller. We are in the process of doing an analysis for a realistic impurity profile. Second, scattering from partially screened ionized impurities has to be properly accounted for. There do exist self-consistent calculations of momentum and energy relaxation times that employ such a realistic potential.[46] Recently, the role of ionized-impurity scattering in a quasi-two-dimensional, quantum confined system was studied by Masselink.[47] He observed an enhancement of scattering in a 2D system compared to bulk material, in agreement with theoretical calculations using a screened Coulomb interaction between electrons and ionized impurities. However, such a realistic description has never been used in the context of weak localization (nor the e-e interaction effect) because the Bethe-Salpeter equation for the Cooperon becomes intractable or at least extremely difficult to solve.

Weak localization is caused by the singular behavior of the Cooperon. The interaction effect is another important phenomenon of quantum transport besides weak localization for which the behavior of both the Cooperon and a related propagator, the diffuson, is decisive. Scattering from partially screened ionized impurities is even more important for understanding the interaction effect. Because both phenomena may contribute to transport properties, uncertainty in determining one of these effects causes likewise uncertainty in the other. In more detailed studies of the interaction effect and its dependence on a carrier distribution, one needs to take into account the doping profile, and a realistic electron-impurity weakly screened long-range potential. This hopefully will allow one to resolve enormous discrepancies existing in the literature (such as a negative value of an effective e-e potential—a clearly unphysical feature for a $GaAs/Al_xGa_{1-x}As$ system).[27]

In summary, this is the first work delivering some evidence for the effect of long-range electron-impurity scattering in the context of a WL correction. The effect is obvious in classical transport. There is mention of it in the electron-electron interaction work of Paalanen, Tsui, and Hwang.[27] These workers consider classically the electron-electron interaction effect correction to the conductivity in high magnetic field $\omega_c\tau_o > 1$, where τ_o is the transport relaxation time. They find general agreement between energy relaxation times from Shubnikov–de Haas oscillations (SdH) and an electron-electron interaction correction to the conductivity. These energy relaxation times are much shorter than the transport relaxation times and this fact is attributed to the inhomogeneous Landau-level broadening by the dominance of long-range potential fluctuations. The electron-electron interaction theory used in their paper also employs the pointlike electron-impurity scattering and accounts for the electron-electron long-range interaction in the lowest order (this procedure is considered by some as inadequate, e.g., Kawaji[27].) In our paper we study the WL correction to conductivity at low magnetic fields, where the electron energy relaxation time is obviously different from the high-B case and where there is no SdH counterpart for comparison.

ACKNOWLEDGMENTS

The samples discussed in this paper were fabricated at Texas Instruments Central Research Laboratories, for which we gratefully acknowledge support. The authors wish to thank Gregory Spencer for the final steps in the sample processing. This material is based in part on work

supported by the Texas Advanced Research Program (Grant No. 999903-136), NASA-SPC Program (Grant No. NAGW-1194), Texas Instruments, Inc. (Grant No. SRA-04023), National Science Foundation (Grant No. DMR 91-07460), and by the U.S.–Poland Sklodowska-Curie Fund. One of the authors (C.J.) acknowledges partial support from the Polish Research Council (Grant No. 2 0401 91 01).

*Permanent address: Department of Physics, Jagellonian University, Cracow, Poland.

[1]See e.g., the review by G. Bergmann, Phys. Rep. **107**, 1 (1984).

[2]P. A. Lee and T. V. Ramakrishnan, Rev. Mod. Phys. **57**, 287 (1985).

[3]L. Pfeiffer, E. F. Schubert, K. W. West, and C. W. Magee, Appl. Phys. Lett. **58**, 2258 (1991).

[4]E. F. Schubert, J. Vac. Sci. Technol. A **8**, 2980 (1990).

[5]A-M. Lanzilotto, M. Santos, and M. Shayegan, Appl. Phys. Lett. **55**, 1445 (1989).

[6]J. E. Cunningham, T. H. Chiu, B. Tell, and W. Jan, J. Vac. Sci. Technol. B **8**, 157 (1990).

[7]F. Stern and W. E. Howard, Phys. Rev. **163**, 816 (1967); T. Ando, A. B. Fowler, and F. Stern, Rev. Mod. Phys. **54**, 437 (1982).

[8]M. A. Reed (private communication).

[9]M. A. Haase, M. A. Emanuel, S. C. Smith, J. J. Coleman, and G. E. Stillman, Appl. Phys. Lett. **50**, 404 (1987).

[10]M. Lee and S. A. Solin, Solid State Commun. **83**, 673 (1992) refer to this calculation from private communication with L. R. Ram-Mohan.

[11]R. de L. Krönig and W. J. Penney, Proc. R. Soc. London Ser. A **130**, 499 (1930).

[12]H. L. Störmer, J. P. Eisenstein, A. C. Gossard, W. Wiegmann, and K. Baldwin, Phys. Rev. Lett. **56**, 85 (1986).

[13]See, e.g., L. L. Chang, H. Sakaki, C. A. Chang, and L. Esaki, Phys. Rev. Lett. **38**, 1489 (1977); E. E. Mendez, L. L. Chang, G. Landgren, R. Ludeke, L. Esaki, and F. H. Pollak, *ibid.* **46**, 1230 (1981); E. Tuncel, L. Pavesi, D. Martin, and F. K. Reinhart, Phys. Rev. B **38**, 1597 (1988).

[14]W. Szott, C. Jedrzejek, and W. P. Kirk, Phys. Rev. B **40**, 1790 (1989).

[15]W. Szott, C. Jedrzejek, and W. P. Kirk, Phys. Rev. B **45**, 3565 (1992).

[16]W. Szott, C. Jedrzejek, and W. P. Kirk, Phys. Rev. B **46**, 15905 (1992).

[17]N. W. Ashcroft and N. D. Mermin, *Solid State Physics* (Holt, Rinehart, and Winston, New York, 1976).

[18]B. R. Nag, *Electron Transport in Compound Semiconductors* (Springer-Verlag, Berlin, 1980).

[19]B. L. Altshuler, D. Khmel'nitzkii, A. I. Larkin, and P. A. Lee, Phys. Rev. B **22**, 5142 (1980); A. Houghton, J. K. Senna, and S. C. Ying, *ibid.* **25**, 2196 (1982).

[20]B. L. Altshuler and A. G. Aronov, in *Electron-Electron Interaction in Disordered Systems*, edited by A. L. Efros and M. Pollak (Elsevier, Amsterdam, 1985), p. 1.

[21]M. J. Uren, R. A. Davies, and M. Pepper, J. Phys. C **13**, L985 (1980); D. J. Bishop, D. C. Tsui, and R. C. Dynes, Phys. Rev. Lett. **46**, 360 (1981).

[22]A. H. Wilson, *The Theory of Metals* (Cambridge University Press, New York, 1953).

[23]M. N. Baibich, J. M. Brotto, A. Fert, F. Nguyen Van Dau, E. Petroff, P. Eitenne, G. Creuzet, A. Friedrich, and J. Chazelas, Phys. Rev. Lett. **61**, 2472 (1988).

[24]D. K. C. MacDonald and K. Sargison, Proc. R. Soc. London Ser. A **203**, 223 (1950).

[25]W. Szott, E. Palm, and W. P. Kirk, Bull. Am. Phys. Soc. **33**, 821 (1988).

[26]S. Kobayashi and F. Komori, Prog. Theor. Phys. Suppl. **84**, 224 (1985).

[27]M. A. Paalanen, D. C. Tsui, and J. C. M. Hwang, Phys. Rev. Lett. **51**, 2226 (1983); S. Kawaji, Prog. Theor. Phys. Suppl. **84**, 178 (1985); D. J. Newson, C. M. McFadden, and M. Pepper, Philos. Mag. B **52**, 437 (1985); K. K. Choi, D. C. Tsui, and S. C. Palmeter, Phys. Rev. B **33**, 8216 (1986).

[28]B. J. F. Lin, M. A. Paalanen, A. C. Gossard, and D. C. Tsui, Phys. Rev. B **29**, 927 (1984).

[29]W. Duncan and E. Schneider, Phys. Lett. **7**, 23 (1963).

[30]S. Kawaji, K. Kuboki, H. Shigeno, T. Nambu, J. Wakabayshi, J. Yoshino, and H. Sakaki, *Proceedings of the 17th International Conference on the Physics of Semiconductors*, edited by J. D. Chadi and W. A. Harrison (Springer-Verlag, Berlin, 1985); J. A. Simmons, D. C. Tsui, and G. Weimann, Surf. Sci. **196**, 81 (1988).

[31]R. Taboryski and P. E. Lindelof, Semicond. Sci. Technol. **5**, 933 (1990).

[32]T. H. Englert, J. C. Maan, G. Remenyi, H. Künzel, K. Ploog, A. Fischer, and A. Briggs, Surf. Sci. **142**, 68 (1984).

[33]J. K. Moyle, J. T. Cheung, and N. P. Ong, Phys. Rev. B **35**, 5639 (1987).

[34]B. Y. Jin and J. B. Ketterson, Phys. Rev. B **33**, 8797 (1986).

[35]S. Hikami, A. I. Larkin, and Y. Nagaoka, Prog. Theor. Phys. **63**, 707 (1980).

[36]B. L. Altshuler, A. G. Aronov, and P. L. Lee, Phys. Rev. Lett. **44**, 1288 (1980).

[37]Y. Kawaguchi and S. Kawaji, J. Phys. Soc. Jpn. **48**, 699 (1980).

[38]H. Fukuyama, J. Phys. Soc. Jpn. **50**, 3562 (1981).

[39]H. Fukuyama, J. Phys. Soc. Jpn. **49**, 649 (1980).

[40]W. Szott, C. Jedrzejek, and W. P. Kirk, Phys. Rev. Lett. **63**, 1980 (1989).

[41]B. L. Altshuler and A. G. Aronov, Pis'ma Zh. Eksp. Teor. Fiz. **33**, 515 (1981) [JETP Lett. **33**, 499 (1981)]; Solid State Commun. **38**, 11 (1981).

[42]B. L. Altshuler, A. G. Aronov, and D. E. Khmel'nitskii, J. Phys. C **15**, 7367 (1982).

[43]A. Schmid, Z. Phys. C **271**, 251 (1974); B. L. Altshuler and A. G. Aronov, Pis'ma Zh. Eksp. Teor. Fiz. **30**, 514 (1979) [JETP Lett. **30**, 482 (1979)].

[44]A. K. M. Wennberg, S. N. Ytterboe, C. M. Gould, H. M. Bozler, J. Klem, and H. Morkoç, Phys. Rev. B **34**, 4409 (1986).

[45]M. L. Roukes, M. R. Freeman, R. S. Germain, R. C. Richardson, and M. B. Ketchen, Phys. Rev. Lett. **55**, 422 (1985).

[46]A. Gold, Phys. Rev. B **38**, 10978 (1988).

[47]W. T. Masselink, Phys. Rev. Lett. **66**, 1513 (1991); Appl. Phys. Lett. **59**, 694 (1991).

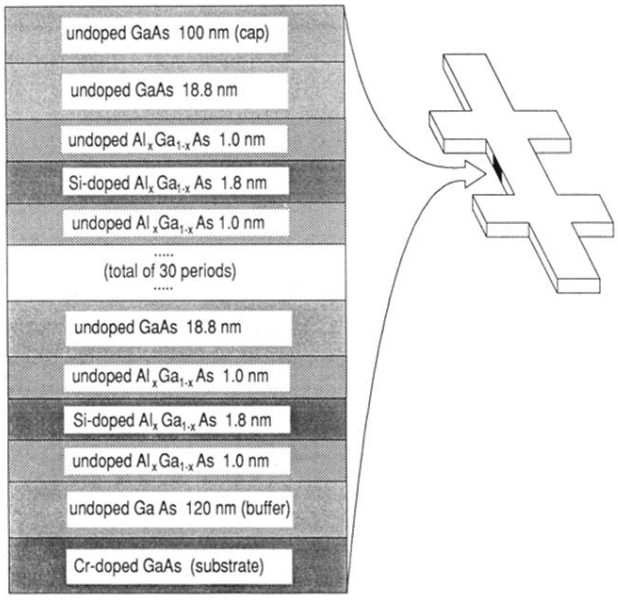

FIG. 1. Cross-sectional view of the superlattice structure.